J. Fluid Mech. (1988), *vol.* 187, *pp.* 467–486
Printed in Great Britain

An investigation of shock/boundary-layer interactions on curved surfaces at transonic speeds

By X. LIU AND L. C. SQUIRE
Cambridge University Engineering Department, Trumpington Street, Cambridge CB2 1PZ, UK

(Received 28 November 1985 and in revised form 4 August 1987)

A detailed experimental investigation has been made of shock/boundary-layer interactions on curved surfaces at transonic speeds. The shock waves were generated above circular-arc models with different radii mounted on the floor of the wind-tunnel test section. The ratio of the boundary-layer thickness ($U/U_e = 0.99$) in front of the shock to the radius of the surface curvature ranged from 0 (i.e. a flat surface) to 0.068. The Mach number just in front of the shock varied from 1.00 to 1.82 and the Reynolds number based on the model chord length was about 1.6 million. Interacting-flow studies include flows with shock-induced separation, flows with trailing-edge separation and flows with no separation. From all these studies it was found that separation was most extensive at the critical peak Mach number at which the separation changes from trailing-edge separation to shock-induced separation.

1. Introduction

With the development of aviation and space flight, the problem of shock/boundary-layer interaction has become more and more important in many practical situations. Examples include the flow around transonic aerofoils, in diffusers of centrifugal compressors or wind tunnels, at centrebody inlets and in turbomachinery cascades. When the shock is strong, it can cause separation and change the overall flow field significantly. This can produce dramatic changes in the aerodynamic characteristics of an aircraft or other aerodynamic device which, if not handled properly, can cause catastrophic problems in flight safety, control effectiveness, or engine efficiency. Since the phenomenon is so important, a large number of investigations have been carried out since the late 1940s as summarized by Green (1970), Korkegi (1971) and Brusseleers (1980). However, owing to the complexity of the problem, our understanding of it is still far from complete and further research, especially experimental measurements, is necessary. For example in many practical problems the interaction takes place at transonic speed on a curved surface where the boundary layer is turbulent and in a highly non-equilibrium condition, having developed in non-zero pressure gradients. However, research on the interaction in such situations has been rather limited, since most of the previous research has been made on the interactions of shock waves with a boundary layer on a flat surface that has developed in approximately zero-pressure-gradient conditions. Although there are some investigations on aerofoils or curved walls, the curvature is not changed in the experiments so that the effect of curvature cannot be studied clearly, and usually the boundary layer is not separated. Thus the shock/boundary-layer interactions with boundary layers developing under non-zero pressure gradient, with different surface curvatures, and with flow separations are still not well understood. This paper presents the results of a detailed experimental investigation of such flows.

As will be shown in the next section the experiments were made in a relatively small tunnel with the interaction of interest taking place on a bump on one wall of the tunnel. This bump spanned the whole width of the test section, but clearly the interaction on it was influenced by the corresponding interactions taking place on the other three walls of the tunnel. The extent to which the interacting flow over the bump surface can be considered as representative of a two-dimensional interaction is considered in §2.2 below.

2. Experimental details

2.1. *General details of the tests*

The experiment was conducted in the blow-down wind tunnel shown in figure 1. The top liner was a flat plate. The bottom liner was carefully padded to give a 0.3° divergence to counteract the boundary-layer development, so that a uniform incoming flow was achieved. The boundary layers developed from the settling chamber along the tunnel walls and were fully turbulent ($R_\theta > 10^4$) in the test region. One of a series of circular-arc models spanning the full width of the tunnel was mounted on the tunnel floor to generate the shock, and an aerofoil was mounted as a second throat to control the shock strength. By setting this second-throat aerofoil to different incidences, the back pressure could be set to any desired value. When the back pressure was set low enough compared with the upstream total pressure, the incoming subsonic flow was accelerated over the circular-arc model to supersonic flow. At certain back pressures, the supersonic flow was terminated by a nearly normal shock standing somewhere on the downstream half of the circular-arc model. Thus the desired transonic shock-wave/turbulent-boundary-layer interaction on a curved surface was generated, as is illustrated in figure 1. At the same time, an interaction on a flat surface was generated on the roof of the tunnel.

For all tests the settling-chamber stagnation pressure was 0.48 Bar (gauge) and the stagnation temperature was close to 290 K. Five circular-arc models with the same chord length of 80 mm but different curvatures were used. The radii of the circular-arc models were 401, 268, 163, 104 and 73 mm and the ratio of the boundary-layer thickness ($U/U_e = 0.99$) in front of the shock to the radius of the surface curvature ranged from 0.015 to 0.068. In addition, on the top flat surface this ratio is zero. For each model, a series of shock waves with different strengths and different positions was generated by setting the second-throat aerofoil to different angles, and in all 68 different test cases were studied. The peak Mach numbers in front of the shock wave varied from 1.00 to 1.82. This covered cases where there was no separation and cases where the boundary layer was extensively separated. Each test case will be referred to by the radius of the circular-arc model R and the second-throat aerofoil setting angle A, but for the cases where the flow on only one surface is concerned the test case will be referred to by R and the peak Mach number M_p which was calculated from the surface static pressure and upstream stagnation pressure using the isentropic relationship.

The main measurements include laser holographic interferometry, schlieren visualization, oil-flow tests, surface-pressure survey, and extensive boundary-layer traverses. The laser holographic technique and the associated equipment are described in detail by Vest (1979) and Bryanstan-Cross & Denton (1982). The boundary-layer profiles were measured by traversing the layer with a single flattened Pitot tube of overall height 0.18 mm. The main traverse mechanism was contained

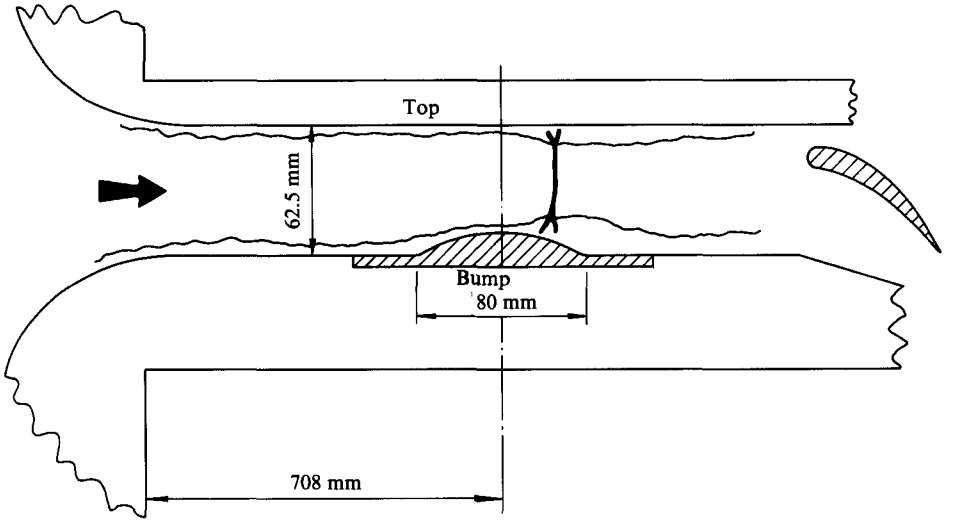

FIGURE 1. Sketch of test section.

within the test surface with only the probe and a small support carrier in the flow.

No motion of the shock was observed in the schlieren system, except in a few cases where some small-amplitude oscillations of the shock foot were observed on the top surface when the Mach number was close to 1. However, overall motion of the shock was observed in dual-exposure holographic interferograms with separation times as short as 1 μs, suggesting that high-frequency oscillations are present. No measurements of these oscillations were made.

2.2. *Two-dimensionality of the flow*

In view of the small scale of the tunnel and particularly the span of the test surface (114 mm) compared with the thickness of the test boundary layer (>5 mm) it is necessary to consider whether the flow near the centreline line of the bump surface is representative of the flow over a similar bump of infinite span. This aspect was studied by surface oil-flow patterns, interferograms obtained by laser holography, pressure distributions on and off the centreline and a momentum balance of boundary-layer measurements made along the centreline.

Typical oil-flow patterns are shown in figures 2 and 3. Figure 2(*a*) shows a flow in which the boundary layer over the bump surface is almost completely attached and it will be seen that the streamlines over almost the whole span are straight and parallel to the tunnel axis. However, with larger regions of separation (figure 2*b*) there are significant regions of three-dimensional flow near the walls although over the inner two-thirds of the span the separation and reattachment lines are straight and normal to the stream direction. Further examples of surface oil-flow patterns are shown in figure 3 where the separation-line positions are compared with the separation positions shown in the corresponding interferograms; the separation position in the interferograms is taken as the point where the fringes near the wall start to widen and turn normal to the surface. As will be seen the separation positions indicated by the two methods are in very good agreement. Noting that the fringes in the interferogram are directly related to changes in the integrated density field across the whole span of the tunnel, this good agreement shows that the three-

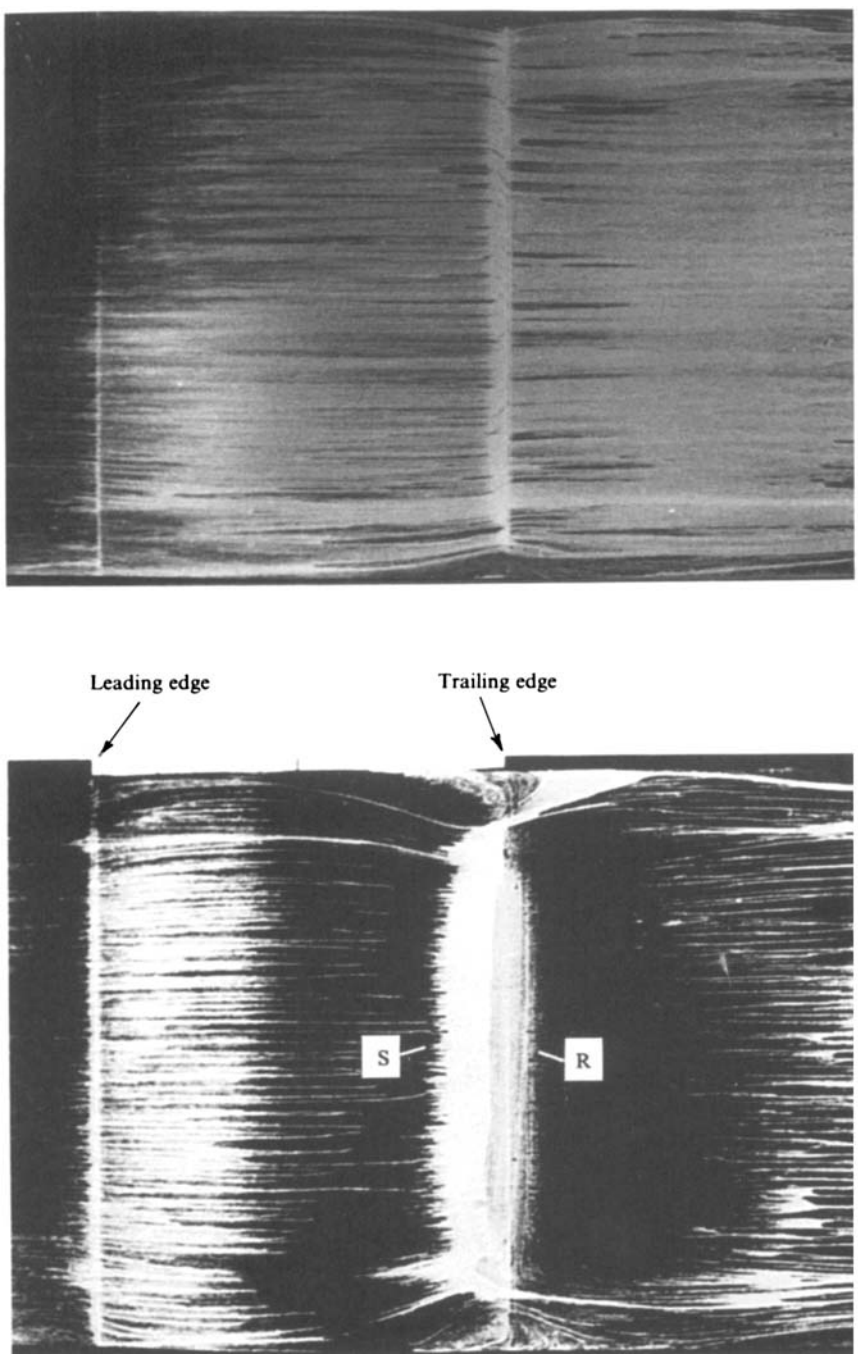

FIGURE 2. Separation and reattachment positions as shown by oil-flow patterns.

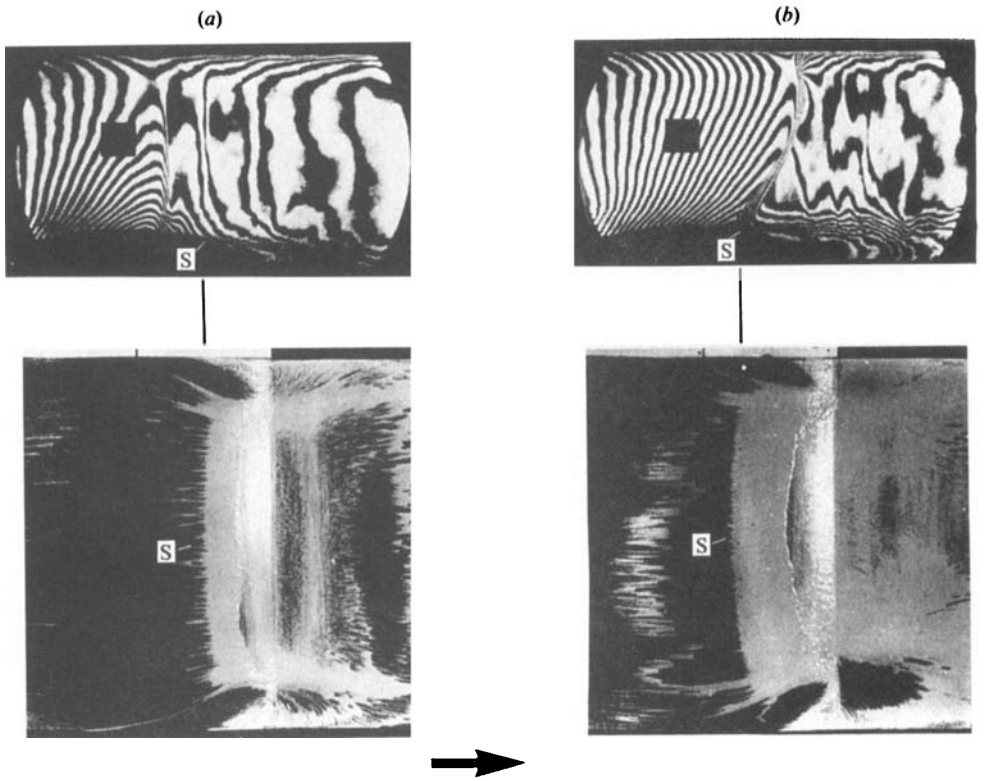

FIGURE 3. The separation position as shown in the oil-flow pattern and in the corresponding interferogram. $R = 104$ mm: (*a*) $A = 11°$; (*b*) 10°.

dimensional effects shown in the oil flow near the wall have a relatively small effect on the density field. Figure 3(*b*) also shows that away from the wall the narrow band of about 10 fringes which corresponds to the increase in density across the shock wave is about 2 mm thick (the black square in the photograph is 10 mm square). A study of off-axis holograms shows that this finite thickness of the shock in the free stream is associated with the sidewall boundary layers, and that outside the boundary layer the shock is straight and normal to the tunnel axis.

Only a few measurements of pressure distributions off the centreline were obtained and most of these were for flows with separation and reattachment. In general the measurements showed that there were some small changes in the pressure distributions away from the centreline, but that there were no gross changes in the nature of the flow.

Figures 4 and 5 show typical results of applying a momentum balance to the boundary-layer measurements. In these figures the points correspond to the measured values of the momentum thickness while the lines correspond to values of momentum thickness obtained by integrating the two-dimensional momentum integral equation

$$\frac{\mathrm{d}\theta}{\mathrm{d}x} = \tfrac{1}{2}c_f - \frac{\theta}{U_\mathrm{e}}\frac{\mathrm{d}U_\mathrm{e}}{\mathrm{d}x}(2+H-M_\mathrm{e}^2)$$

using measured values of U_e, M_e, H and c_f. In each of the figures the chain dotted line corresponds to the measured ('isentropic') Mach number at the edge of the

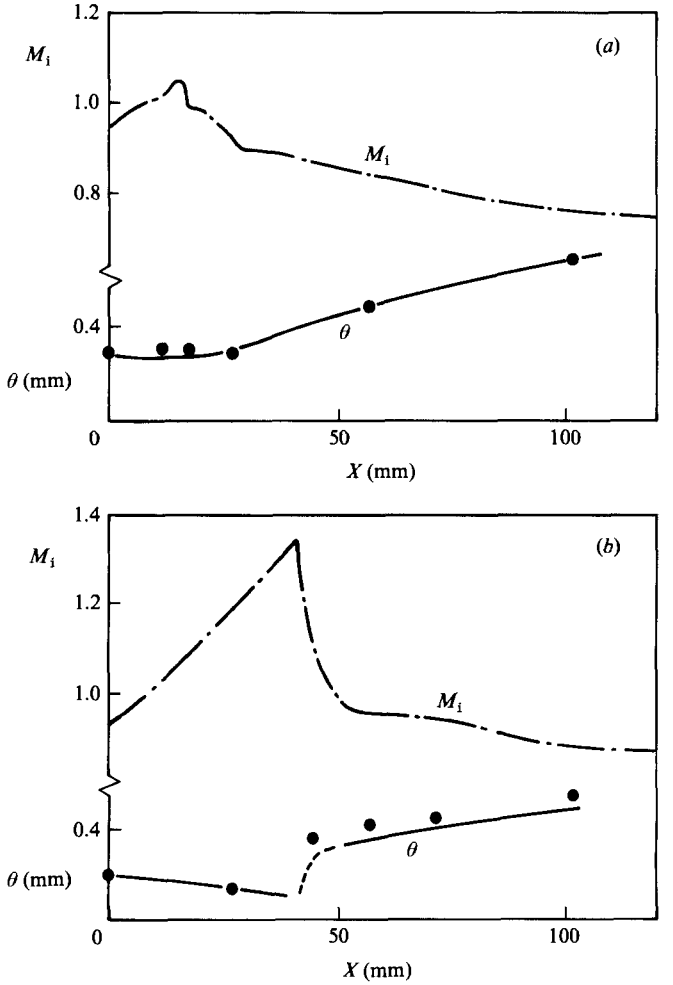

FIGURE 4. Momentum balance on the flat top surface: ●, measured θ; —, θ from two-dimensional momentum integral equation using measured values of U_e, M_e, H and c_f; —·—, measured 'isentropic' Mach number.

boundary layer. Figure 4 shows two cases for boundary-layer measurements along the centreline of the flat top surface of the tunnel. In figure 4 (a) the flow is completely attached with the Mach number just becoming sonic. As will be seen the measured momentum thickness appears to be accurately two-dimensional for the whole layer. Figure 4 (b) shows a case where the Mach number reaches 1.33 with a stronger shock and a small region of separation. In this case there were not sufficient measurements to obtain an accurate solution of the momentum integral equation across the separated region so an approximate momentum analysis due to Baker (1980) was used. Ahead of the shock the measured boundary layer is accurately two-dimensional, but Baker's analysis underestimates the increase in momentum thickness across the shock. However, the calculated growth of the momentum thickness downstream of the shock follows the measured growth very closely. In fact if the calculations are restarted using the measured value at $X = 42$ there is exact agreement between the measured and calculated values for the rest of the development. Figure 5 (a, b) shows

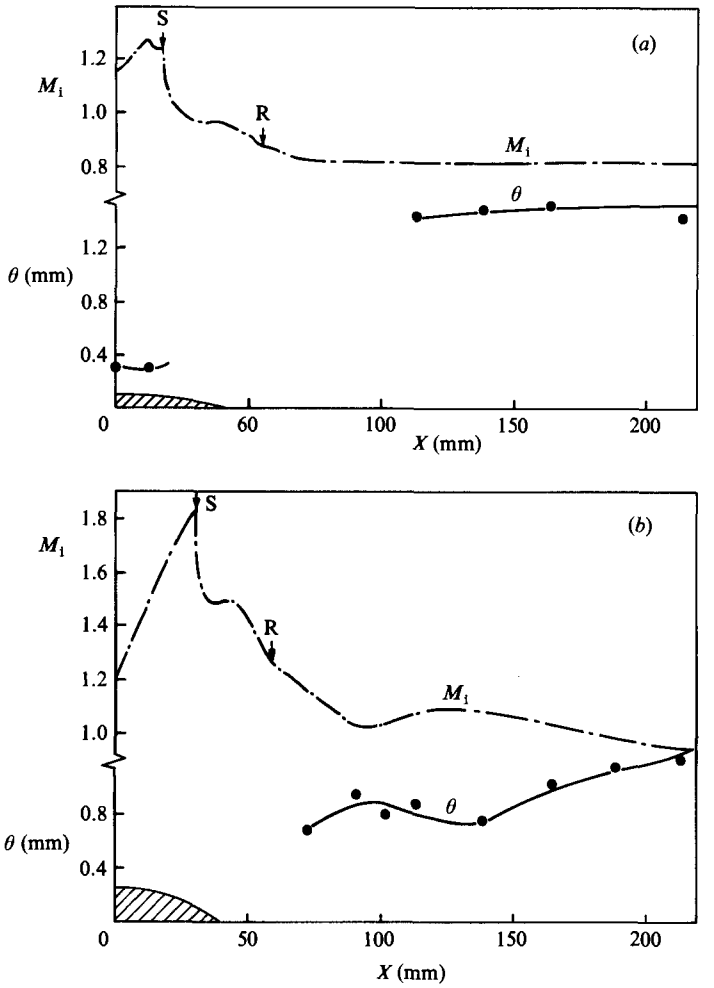

FIGURE 5. Momentum balance on the bump surface. ●, measured θ; —, θ from two-dimensional momentum integral equation using measured values of U_e, M_e, H and c_f; —·—, measured 'isentropic' Mach number.

two developments on the bump surface where there are extensive regions of separation. In figure 5(*a*) there are two measured values upstream of the shock and the jump to the high values downstream of the shock is too large to be bridged by any approximate analysis. Thus the calculated values downstream of the shock use the measured value at $X = 114$ as initial condition. Except for the last point the two-dimensionality is satisfactory. Figure 5(*b*) shows an extreme case of the boundary-layer development downstream of the largest bump when the peak Mach number reaches 1.8. The first few measured profiles appear erratic and are probably affected by the reattachment process; however, further downstream the flow is again accurately two-dimensional.

Taken together these results suggest that for attached flows and for flows with small regions of separation measurements along the tunnel centreline are representative of two-dimensional flow over the bump surfaces. However, in flows with larger regions of separation the flow in the separation region is clearly affected by the

presence of the walls and in particular by the shock interaction with the boundary layers on the sidewalls. Even in these cases the measured boundary-layer development well downstream of reattachment satisfies the two-dimensional momentum integral equation.

3. The general features of the flow field

3.1. *Flow structure*

For each model a series of flow patterns was produced by changing the back pressure. Figure 6(*a–h*) is interferograms showing the development of the flow structure with decreasing back pressure. The fringes in the interferograms are density contours. The black square shows the dimension, with each side 10 mm long and with the downstream edge lined up with the mid-chord position of the bump. When the back pressure is high (figure 6*a*), the whole flow field is subsonic. As the back pressure decreases, the incoming free-stream Mach number increases, and a supersonic zone terminated by a normal shock appears above the circular-arc model (figure 6*b*). With further decrease of the back pressure, the free-stream Mach number increases, the supersonic region expands and the normal shock moves downstream. Eventually the sonic line reaches the top liner and the flow chokes (figure 6*c*). Further decrease in the back pressure has no influence on the pressure distribution upstream of the sonic line, but the shock moves further downstream and grows until it reaches the top liner. At this point a nearly normal shock spanning the tunnel height is formed (figure 6*d*), and the flow downstream of the shock is subsonic. As the back pressure decreases still further, the shock becomes bifurcated and a lambda shock is formed (figure 6*e*). The lambda foot gets bigger until a Mach reflection forms (figure 6*f*). With further decrease in the back pressure, the shock becomes more oblique (figure 6*g*) and finally is reflected from the top liner in a regular reflection and the flow behind the shock is supersonic (figure 6*h*).

When the curvature of the circular-arc model is large, high Mach numbers are achieved in front of the shock, and the boundary layer separates extensively forming a very obvious lambda shock. However, when the curvature of the circular-arc model is small, the shock strength is weak and no lambda shock is observed, as for the cases $R = 268$ and 401 mm ($\delta/R = 0.015$ and 0.022).

3.2. *Surface static-pressure distribution*

The surface static-pressure distributions on the top and on the bump surface normalized by the settling-chamber total pressure are plotted in figure 7(*a*, *b*) for several test cases on the model with a radius of 73 mm ($\delta/R = 0.068$). M_p is the peak isentropic Mach number and c is the chord length of the model. The origin of the X-coordinate is set at the mid-chord position of the circular-arc model. The shape of the circular-arc model and a line showing the sonic condition, i.e. $P/P_0 = 0.528$, are also drawn on the figures. (The Mach numbers marked on the right-hand axis are based on the isentropic relations.) The pressures on the bump and the pressures on the top represented by the same symbols were taken during the same tunnel run. The separation and reattachment positions obtained from the oil-flow test are also shown in the figures by the arrows. On the curved surface when the peak Mach number is greater than 1.30, the pressure distributions upstream of the sonic point collapse onto a single line, which shows that the flow is choked. For cases with high peak Mach numbers, there is a region of nearly constant pressure preceded by a sharp pressure

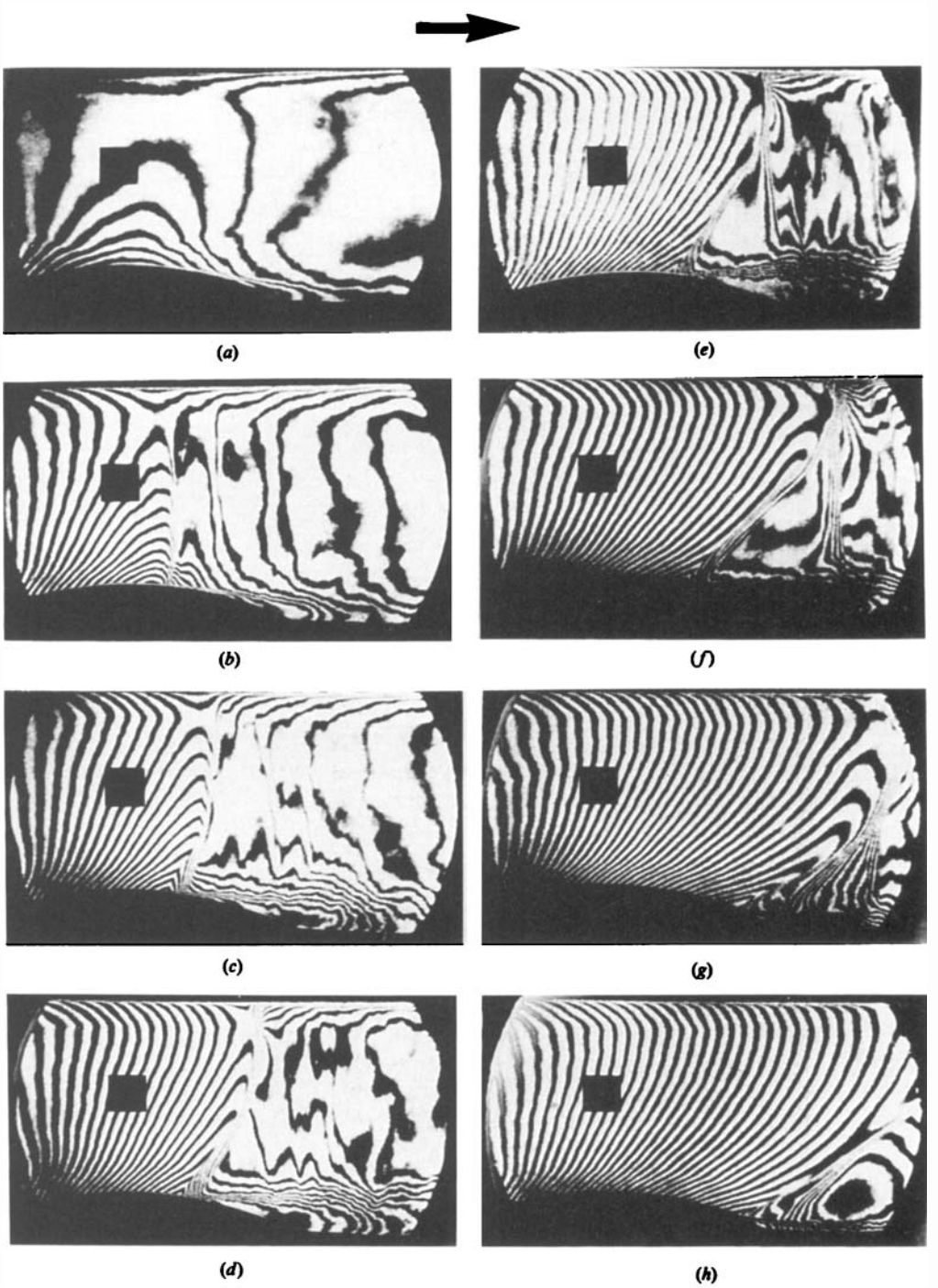

FIGURE 6. Development of the flow with decreasing back pressure.

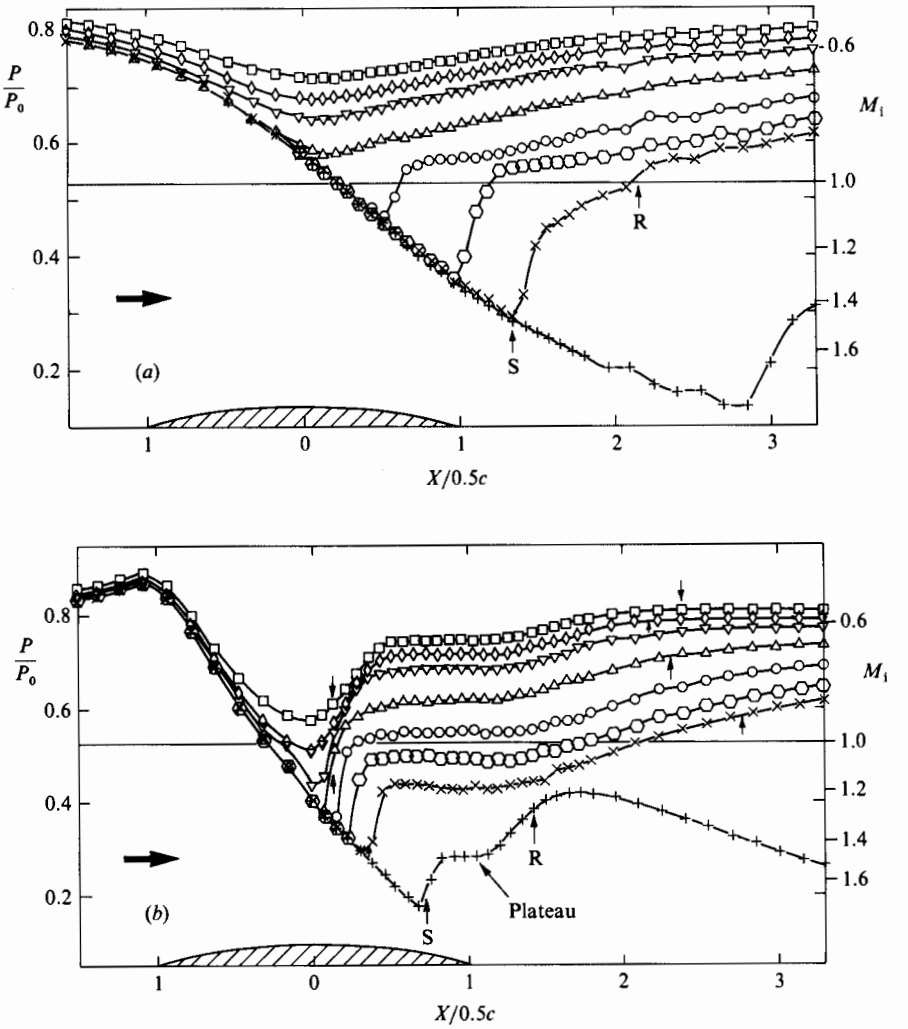

FIGURE 7. Pressure distributions for the case with $R = 73$ mm. (*a*) Top surface: +, $M_p = 1.96$; ×, 1.45; ○, 1.31; ○, 1.10; △, 0.93; ▽, 0.83; ◇, 0.78; □, 0.72. (*b*) Bump surface: +, $M_p = 1.81$; ×, 1.44; ○, 1.36; ○, 1.30; △, 1.27; ▽, 1.17; ◇, 1.04; □, 0.94.

rise. The nearly constant pressure region will be referred to as the plateau, as shown in figure 7(*b*), where S and R are the positions of separation and reattachment respectively obtained from the oil flow test. It is seen that the plateau corresponds to the main part of the separation bubble. The sharp pressure rise between the peak-Mach-number point and the beginning of the plateau will be referred to as the initial compression. Comparing these pressures with the corresponding interferograms in figure 8 and figure 9, it is seen that if at the end of the initial compression the flow is subsonic or the plateau is a subsonic region, only a single shock is produced and the initial compression is just underneath the shock foot, as happens in the case $R = 73$ mm, $M_p = 1.30$ (figure 8). On the other hand if at the end of the initial compression the flow is supersonic or the plateau is a supersonic region, a lambda shock pattern is produced and the initial compression corresponds to the leading oblique shock, as happens in the case of $R = 73$ mm, $M_p = 1.36$ (figure 9). In figure 7

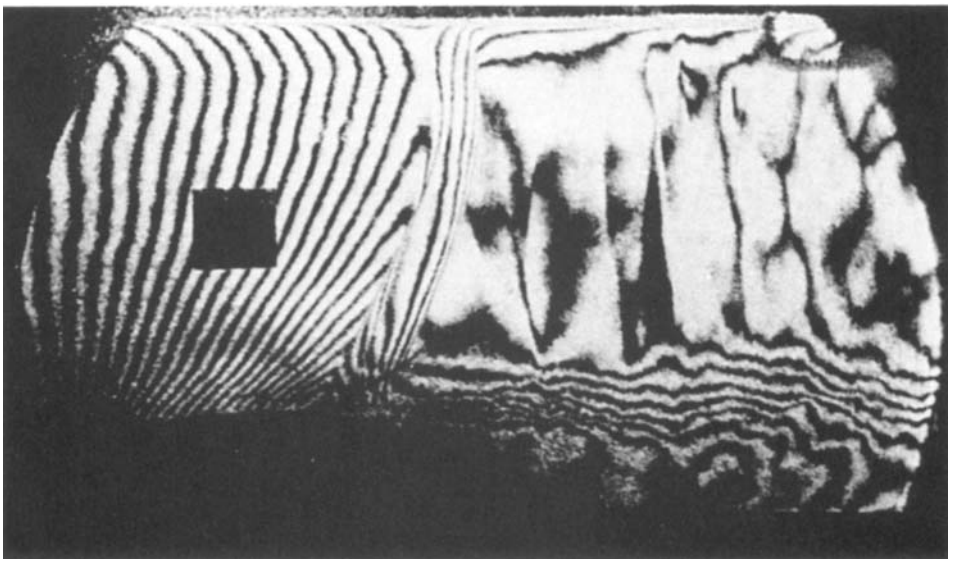

FIGURE 8. The subsonic 'plateau', $R = 73$ mm, M_p (on bump) = 1.30.

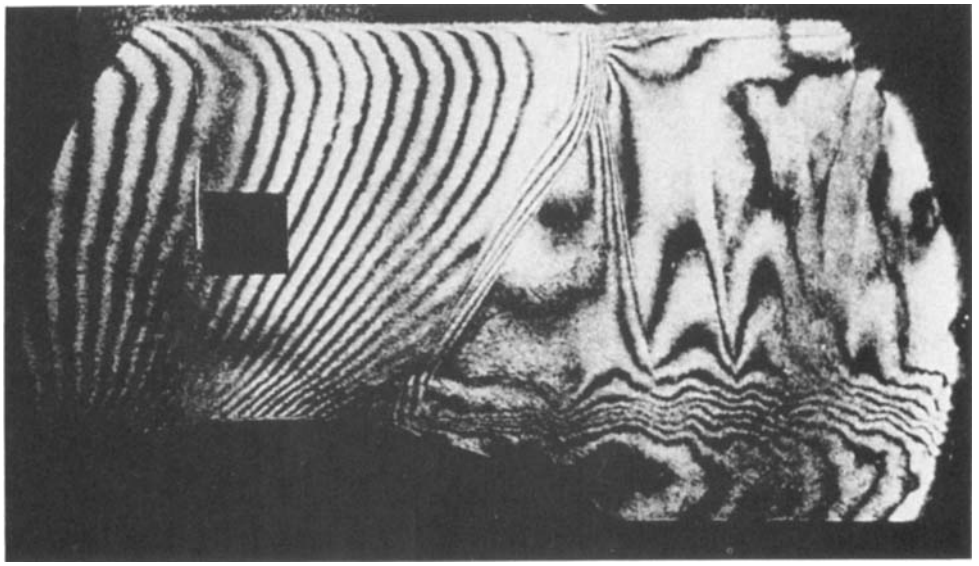

FIGURE 9. The supersonic 'plateau', $R = 73$ mm, M_p (on bump) = 1.36.

it is interesting to note that in the initial compression the pressure gradients for all the choked cases are nearly the same and the pressure increases nearly linearly. The pressure rise up to the plateau, i.e. the difference between the plateau pressure and the minimum pressure, decreases as the peak Mach number increases. The plateau pressure also decreases with increasing peak Mach number. After the plateau, the flow is further compressed during the reattachment process. When the plateau is in a supersonic region, the reattachment process turns the supersonic flow parallel to the flat floor and compresses the flow to subsonic. If the plateau is in a subsonic region the height of the separation bubble becomes smaller in the reattachment

process and the stream tube outside the boundary layer expands so that the flow undergoes subsonic compression just like the subsonic flow around the trailing edge of an aerofoil. After reattachment, the boundary displacement thickness decreases before it increases again. In this region the stream tube is expanding leading to further subsonic compression. Hence whether the plateau is supersonic or subsonic the pressure always increases through reattachment. The pressure distributions have similar shapes for all cases, except for the case $M = 1.81$ where after the reattachment the flow still remains supersonic and so starts accelerating.

The results on other models show that as the curvature of the model decreases, the plateau gets less distinct until finally it disappears for the models with $\delta/R < 0.02$.

Pressure distributions on the top liner have similar characteristics to those of the corresponding pressure distributions on the curved surface. However, the plateau in the pressure distribution is hardly observed, because on this flat surface the flow is either attached or just separated.

4. Analysis of the holographic interferogram

4.1. *Qualitative information*

The double-exposure holographic interferograms were obtained by making two holographic exposures on the same photographic plate, the first before the start of the tunnel run and the second during the tunnel run. A typical interferogram is shown in figure 10 which corresponds to the case $R = 163$ mm and $M_p = 1.27$ on the bump. Outside the boundary layer and upstream of the shock, the stagnation pressure and density are constant. Therefore, in this region the fringes are also Mach-number and static-pressure contours. It is seen that upstream of the shock the fringes are spaced much closer near the bump than near the top. This shows that the flow accelerates faster on the bump than on the top. In the main flow the fringes are nearly straight, but close to the walls the fringes are deflected into the upstream direction. This turning point corresponds to the edge of the boundary layer. From the interferogram it can be seen that there is a very thin layer close to the wall surface in which several fringes are squashed together. From the difference between the wall density calculated from the wall pressure and the wall temperature and the density at the edge of the thin layer obtained from the interferogram, it is deduced that six fringes should be expected in this layer. The thickness of this layer is about 0.5 mm and the fringes are too close to be distinguished. However, this thin layer is not observed in the separated region. From the interferogram, the shape of the shock wave is seen clearly. The main part of the shock in the outer flow is approximately normal and is quite thin. Close to the walls the shock turns towards the upstream direction and the shock is spread out owing to the shock/boundary-layer interaction. At the shock foot the fringe spacing increases gradually in the downstream direction. There is no clear distinction between the oblique shock and the following compression fan. In the separated region the fringes are wide and the spacings large. The fringes run into the wall vertically. Around the separation point the fringes close to the surface change from parallel to the surface to normal to the surface. Around the reattachment point the fringes change from normal to parallel again. As is seen, neither of these processes is an abrupt phenomenon, and in particular the reattachment is a very gradual process. It is very interesting to notice that the thin layer close to the wall leaves the surface after the shock and looks like a free shear

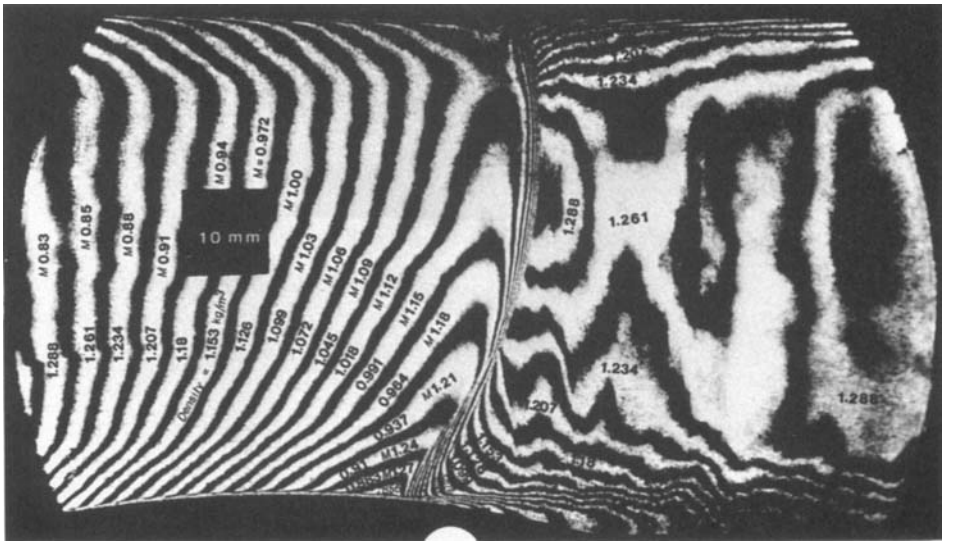

FIGURE 10. Interferogram of the case with $R = 163$ mm, second-throat angle 9°.

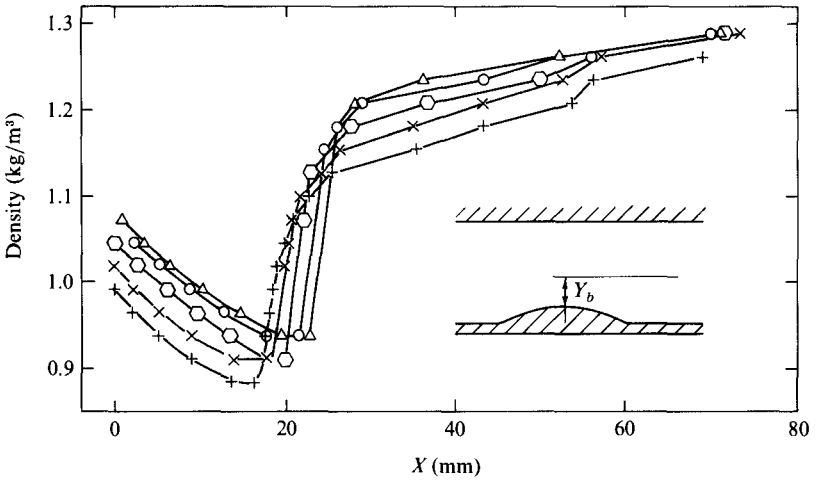

FIGURE 11. Density distributions for the case $R = 163$ mm, second-throat angle 9°. +, $Y_b = 2.15$ mm; ×, 4.41; ⬡, 6.47; ○, 8.62; △, 10.78.

layer above the separation bubble. Downstream of the main shock, there are some very wide irregular fringes showing some non-uniformity, but further downstream the flow becomes more uniform.

4.2. *Quantitative information*

Using standard methods (Vest 1979), the density change $\Delta\rho$ across each fringe shift is calculated to be 0.027 kg/m^3. Thus starting from a point of known density, the density distribution throughout the flow field can be obtained by counting the fringes. A typical result is shown on figure 10 where the density value on each fringe is marked. Upstream of the shock, the numbers preceded by M are the Mach numbers

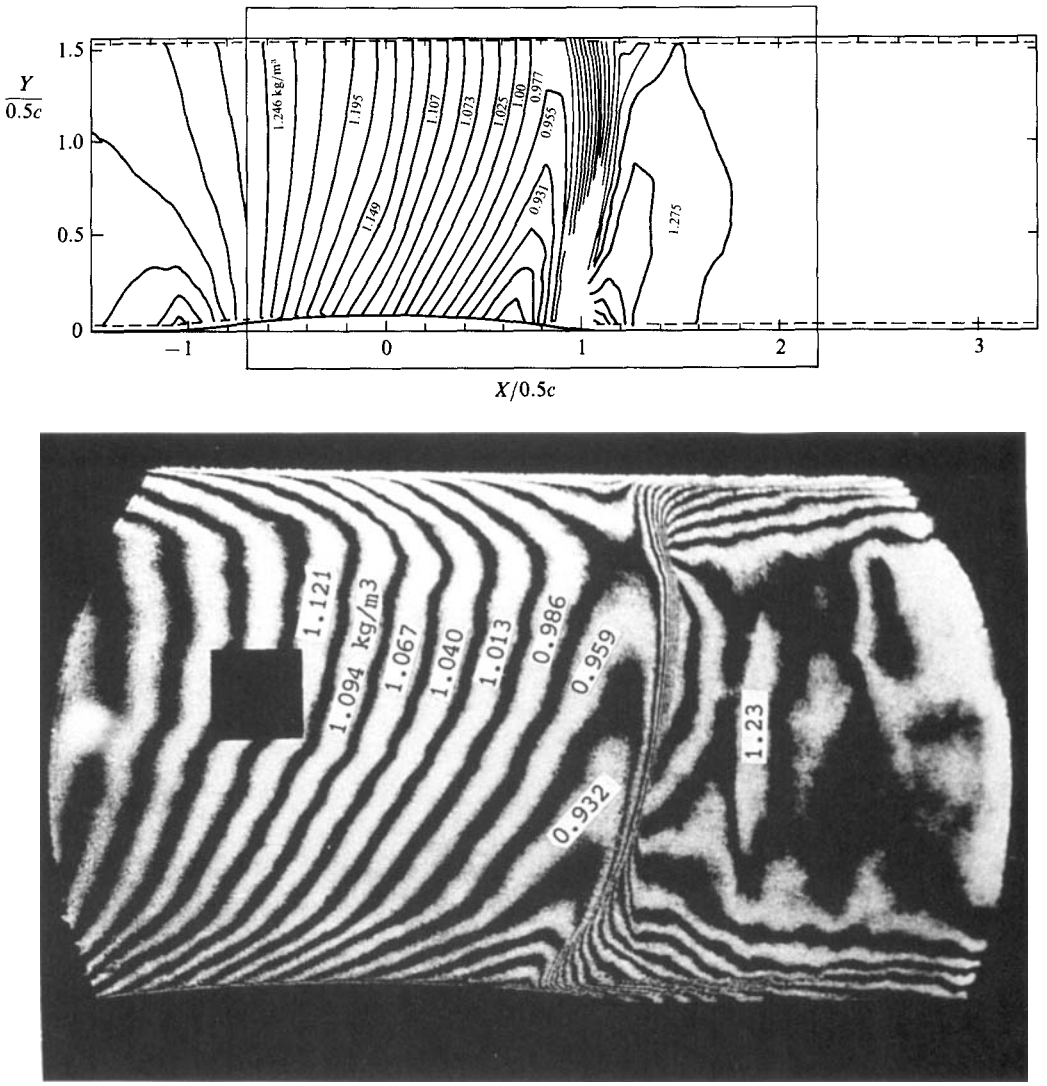

FIGURE 12. Comparison of the calculated density contours with the interferogram. $R = 268$ mm, M_p (on the bump) = 1.31.

calculated from the static density and the settling-chamber density using the isentropic relation. Therefore it represents the Mach number outside the boundary layer.

Figure 11 shows the density distributions along straight lines parallel to the top linear surface. Y_b is the distance from the mid-chord point on the circular-arc-model surface to the line on which the density is measured. The characteristics of the shock/boundary-layer interaction are shown well in this figure. As the distance from the wall surface increases, the streamwise density gradient gets bigger and the spread of the compression gets smaller. Outside the boundary layer the density jumps across the shock nearly as in inviscid flow. However no singular behaviour at the boundary-layer edge corresponding to the after-shock expansion observed by Ackeret (1947) is seen.

It is of interest to compare the density field obtained from the interferogram, as described above, with the results from numerical calculations. For this purpose the whole interacting flow field was calculated by combining an inviscid calculation method with a boundary-layer calculation. The boundary layer was calculated by the lag-entrainment method (Green, Weeks & Brooman 1972) using the measured surface-pressure distribution. The wall surfaces were modified by the boundary-layer displacement thickness and then the main flow was calculated by a time-marching Euler-solver (Denton 1983). A typical calculated result is shown on figure 12 where the predicted density contours are compared with the interferogram. As can be seen, the agreement in the inviscid part of the flow field is good. This agreement provides further confirmation for the two-dimensionality of the flow.

5. Separation

The separation and reattachment positions were obtained from oil-flow patterns as shown in figure 2, where the beginning of the accumulation of the titanium dioxide is taken as the separation position S and the end of this accumulation is taken as the reattachment position R.

Typical separation and reattachment positions on one of the circular-arc models for different peak Mach numbers are shown in figure 13. The shock positions are also shown on the figure. Similar figures were obtained for other models. It is seen that as the peak Mach number increases, the shock moves downstream, while the separation position first moves upstream until it meets the shock and then moves downstream with the shock. The reattachment position first moves downstream with increasing Mach number, but then starts to move upstream at the same peak Mach number as that at which the separation position meets the shock position. These results suggest that when the peak Mach number is small, the shock is not strong enough to cause separation, and the boundary layer separates at some distance downstream of the shock around the trailing edge. This type of separation is caused by the adverse pressure gradient around the trailing edge and will be called trailing-edge separation. As the peak Mach number increases, the separation bubble grows in both upstream and downstream directions and eventually the shock is strong enough to separate the boundary layer just under the shock foot. This type of separation will be called shock-induced separation. For each circular-arc model there is one peak Mach-number value at which the separation changes from trailing-edge separation to shock-induced separation. This peak Mach number will be called the critical peak Mach number. In figure 13 this critical peak Mach number corresponds to the turning point of the separation line, i.e. the point at which the separation point reaches its furthest upstream position. In the present experiment the flow reattached downstream of the trailing edge for all the shock-induced-separation cases. There may be some intermediate cases where after shock-induced separation the boundary layer reattaches before the trailing edge, and then separates again as the trailing edge is approached, but they are not observed in the present experiment.

Figure 14 summarizes the results of all the separation studies. In this figure the critical peak Mach numbers, as deduced from figures similar to figure 13, are plotted by elongated points, where the height of the point denotes the uncertainty of the measurements. It is immediately clear that the critical peak Mach number is almost independent of δ/R, and within the accuracy of the present experiment may be taken as 1.30 for all values of δ/R. When the peak Mach number is greater than 1.3 the separation is always of the shock-induced type. Below $M_p = 1.3$ the flow is

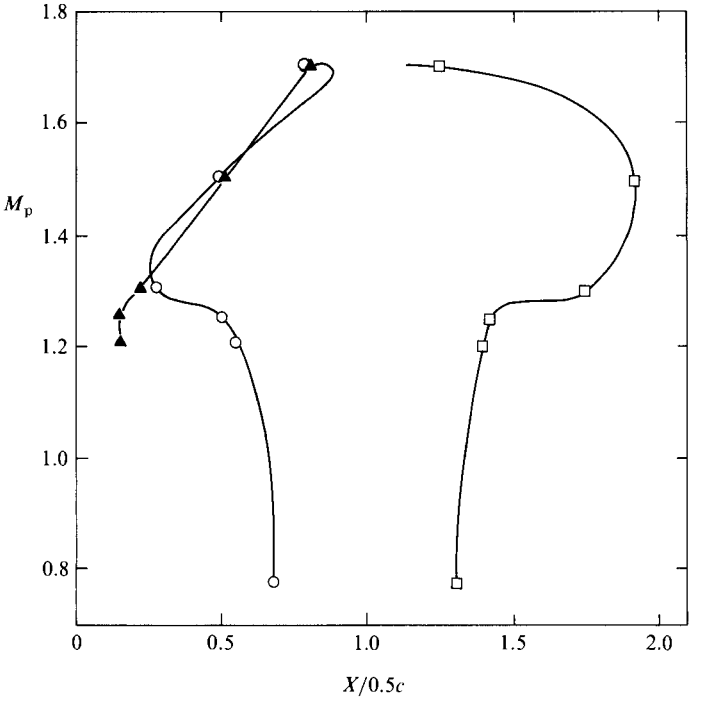

FIGURE 13. The position of the shock (▲), separation (○), and reattachment (□) on the bump with $R = 104$ mm.

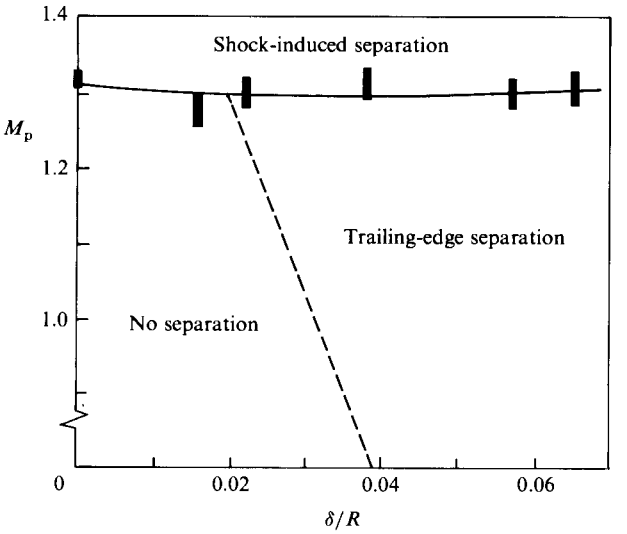

FIGURE 14. Separation boundaries. I, Critical peak Mach numbers as deduced from figures similar to figure 13.

unseparated for small values of δ/R, and for higher values of δ/R trailing-edge separation occurs. The tentative boundary between the separated and unseparated flow is shown by the dashed line in figure 14. The interoferograms showed that at the critical Mach numbers the shocks were all normal shocks, while the surface Mach-number distributions reveal that in most cases the plateau in the pressure

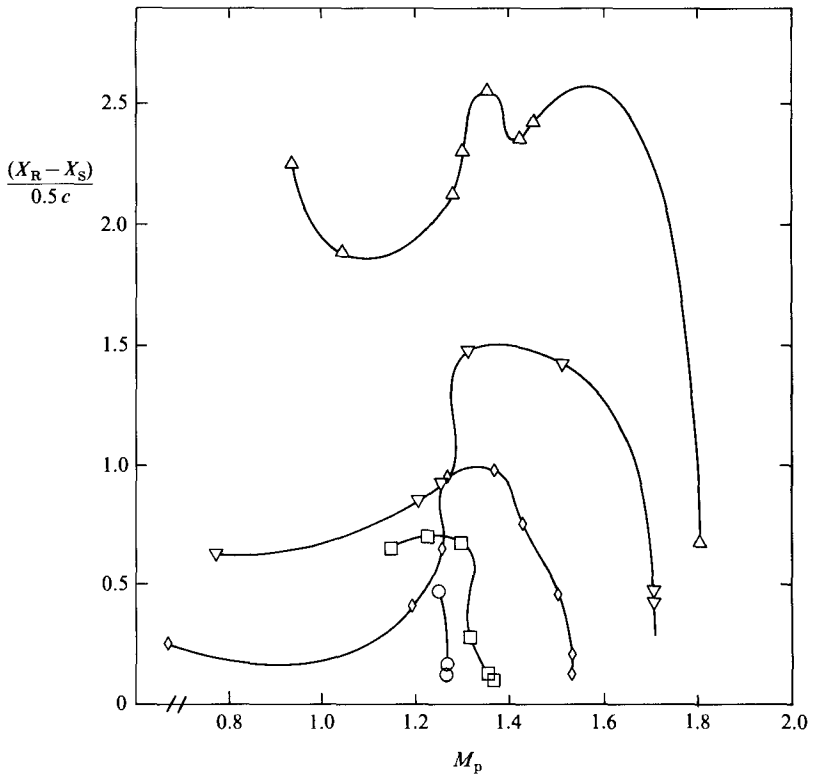

FIGURE 15. Separation lengths on the bumps. △, $R = 73$ mm; ▽, 104; ◇, 163; □, 268; ○, 401.

distribution is subsonic for trailing-edge separation and is supersonic for shock-induced separation.

The separation length, defined as the distance between the separation point and the reattachment point, is shown in figure 15. For each surface curvature, when the peak Mach number is lower than the critical peak Mach number, the separation is trailing-edge induced. The adverse pressure gradient around the trailing edge is increased with increasing peak Mach number so that the separation length increases with peak Mach number. However when the peak Mach number is greater than the critical peak Mach number, the separation is shock-induced. The separation point moves downstream towards the trailing edge together with the shock. This shortens the distance over which the adverse pressure gradient around the trailing edge is acting. As a result, the reattachment point moves upstream and the separation length decreases. Hence the separation length, and the size of the separation bubble, reaches a maximum around the critical peak Mach number for each surface radius. The development of the separation bubble is clearly seen in the holographic interferograms on figure 16 where the flow fields on the $R = 104$ mm model with peak Mach numbers smaller than, equal to and greater than the critical peak Mach number of the circular-arc model are shown.

It can also be seen from figure 15 that with the same peak Mach number the separation length increases with surface curvature. This increase in length of separation occurs because the increase in surface curvature increases the stability of the boundary layer and hence decreases the turbulent fluctuations and the shear

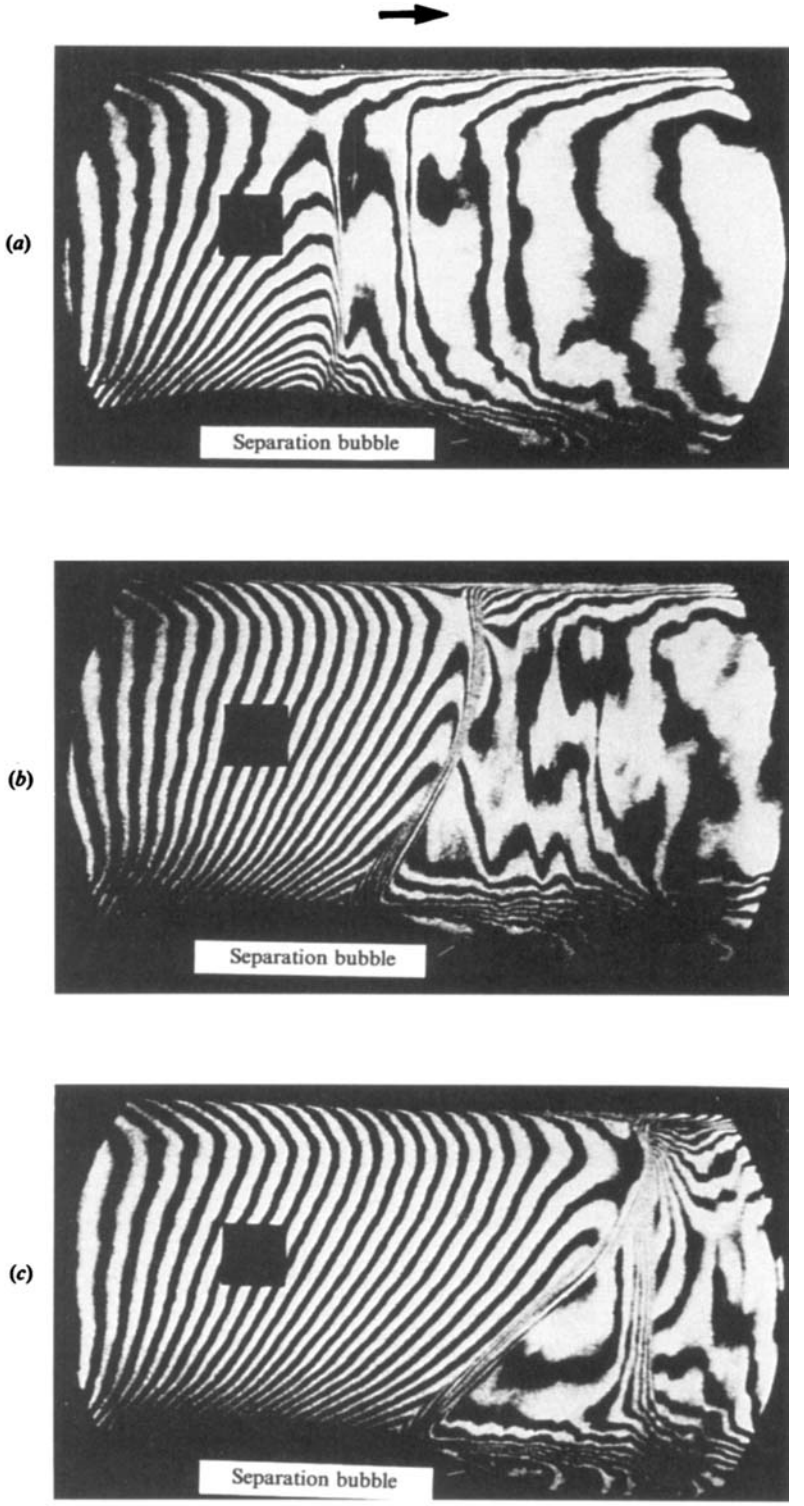

FIGURE 16. Development of the separation bubble on the bump with $R = 104$ mm. (*a*) $A = 11°$, $M_p <$ critical M_p, trailing-edge separation; (*b*) $A = 10°$, $M_p =$ critical M_p, the changeover of separation type; (*c*) $A = 9.25°$, $M_p >$ critical M_p, shock-induced separation.

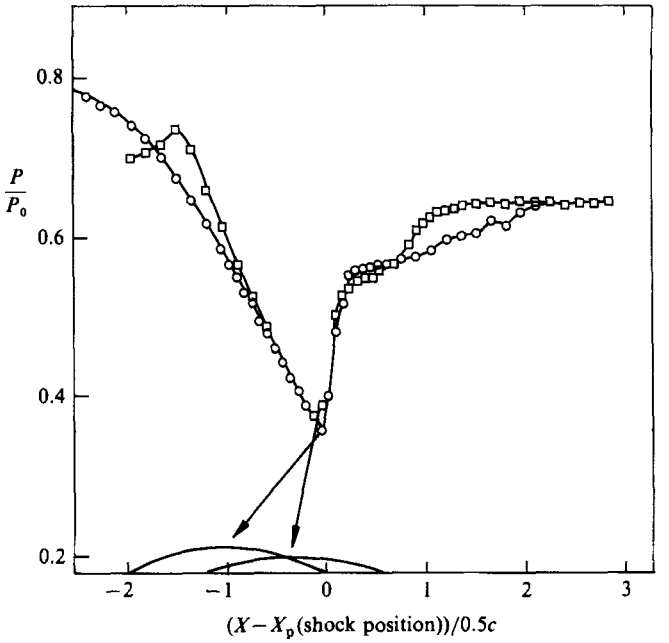

FIGURE 17. Two cases with similar pressure distributions: □, on the bump surface with $R = 163$ mm; ○, on the flat top surface.

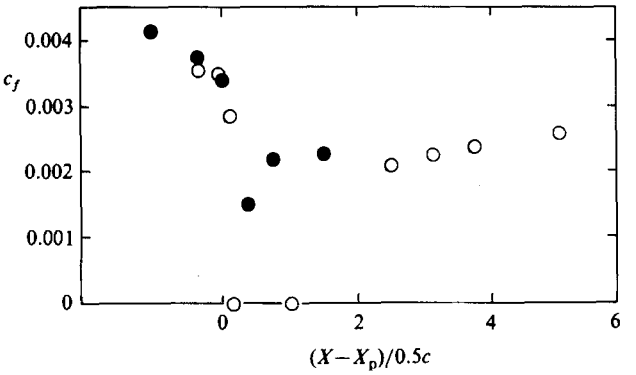

FIGURE 18. The skin-friction development for the two cases with similar pressure distributions: ○, on the curved bump surface with $R = 163$ mm; ●, on the flat top surface.

stress. This trend is confirmed by the results shown in figures 17 and 18. Figure 17 shows two pressure distributions, one on the flat surface and one on a curved surface. In both cases the origin of the x-coordinate is set at the shock position X_p. As will be seen the pressure distributions around the shock position are almost identical, yet the measured skin-friction coefficients are completely different (figure 18) and the boundary layer on the curved surface shows extensive separation, whereas that on the flat surfaces is completely attached.

6. Conclusions

The shock/boundary-layer interaction on curved surfaces at transonic speeds has been studied in detail by laser holographic interferometry, oil flow, surface-pressure distributions and boundary-layer traverses. One important consequence of the shock/boundary-layer interaction is boundary-layer separation which in external flow means lift reduction and possible stall, while in internal flow separation leads to an increase in losses and possible instability. The main results of the present study are summarized by the separation boundaries presented by figure 14. This figure shows that the critical peak Mach number does not change very much with the surface curvature and is close to 1.30 for values of $\delta/R < 0.068$. Hence the well-established rule that shock-induced separation can be avoided by restricting the peak Mach number to less than 1.3 is shown to be true for a wide range of surface curvature. Another important conclusion of the present research is that the separation becomes most severe at the critical peak Mach number at which the separation changes from trailing-edge separation to shock-induced separation.

The authors thank Dr P. J. Bryanston-Cross for much help and advice on the use of the holographic interferometric system. The first author is grateful for the financial support provided by the Government of the People's Republic of China, Cambridge University and Trinity College, Cambridge.

REFERENCES

Ackeret, J., Feldmann, F. & Rott, N. 1947 Investigation of compression shocks and boundary layers in gases moving at high speed. *NACA TM*-1113.

Baker, C. J. 1980 The prediction of boundary layer development through a normal shock wave turbulent boundary layer interaction. *CUED/A-AERO/TR* 10 (1980).

Brusseleers, M. 1980 Physical and numerical aspects of shock boundary layer interaction. V.K.I. L.S. 1980–8.

Bryanston-Cross, P. J. & Denton, J. D. 1982 Comparison of interferometric measurements and computed flow around a wedge profile in the transonic region. *ASME paper* 82-GT-258.

Denton, J. D. 1983 An improved time-marching method for turbomachinery flow calculation. *Trans. ASME* A: *J. Engng for Power* **105**, 514.

Green, J. E. 1970 Interactions between shock waves and turbulent boundary layers. *Prog. Aerospace Sci.* **11**, 235.

Green, J. E., Weeks, D. J. & Brooman, J. W. F. 1972 Prediction of turbulent boundary layers and wakes in compressible flow by a lag-entrainment method. *RAE TR* 72231.

Korkegi, R. H. 1971 Survey of viscous interactions associated with high Mach number flight. *AIAA J.* **9**, 771.

Vest, C. M. 1979 *Holographic Interferometry*. Wiley.